LAWRENCE
LIVERMORE
NATIONAL
LABORATORY

# Electronic Structure of Dense Plasmas by X-ray Scattering

G. Gregori, S. H. Glenzer, F. J. Rogers, S. M. Pollaine, D. H. Froula, C. Blancard, G. Faussurier, P. Renaudin, S. Kuhlbrodt, R. Redmer, and O. L. Landen

## October 7, 2003

# Electronic structure of dense plasmas by x-ray scattering

G. Gregori,* S. H. Glenzer,* F. J. Rogers,* S. M. Pollaine,* D. H. Froula,* C. Blancard,† G. Faussurier,† P. Renaudin,† S. Kuhlbrodt,‡ R. Redmer,‡ and O. L. Landen*
(Dated: October 7, 2003)

We present an improved analytical expression for the x-ray dynamic structure factor from a dense plasma which includes the effects of weakly bound electrons. This result can be applied to describe scattering from low to moderate Z plasmas, and it covers the entire range of plasma conditions that can be found in inertial confinement fusion experiments, from ideal to degenerate up to moderately coupled systems. We use our theory to interpret x-ray scattering experiments from solid density carbon plasma and to extract accurate measurements of electron temperature, electron density and charge state. We use our experimental results to validate various equation-of-state models for carbon plasmas.

## I. INTRODUCTION

X-ray scattering of solid density plasmas has recently been proven a successful technique for the characterization of low-Z warm and dense states of matter [1–3]. In particular, it was shown that by extending the theory of spectrally resolved Thomson scattering to the hard x-ray regime, accurate measurements of the electron temperature, electron density and ionization state can be obtained. In this respect, comparison of the experimental results with equation of state (EOS) models has started revealing important insights on the microscopic electronic state of solid density beryllium plasmas [2]. In this paper, we present a generalization of the technique to higher Z materials, thus allowing the study of basic plasma parameters and transport properties of a vast range of plasma regimes, as the ones created in high energy density experiments relevant for inertial confinement fusion (ICF) [4] and found in the interior of stars and planets.

The x-ray dynamic form factor, which is the fundamental quantity describing the scattering cross section, contains three major contributions that arise from scattering from free electrons, weakly bound and tightly bound electrons. The first term is usually described within the random phase approximation (RPA) [5, 6] and it refers to photon scattering from density fluctuations of the free electrons in the plasma. During the process, energy is exchanged from the photons to the electrons, and the scattered photons are downshifted in energy by the Compton effect. For weakly bound electrons the incident x-ray photons have a certain probability to transfer a portion of their energy and momentum to the electrons, resulting in the appearance of a secondary inelastic scattering feature in the spectrum of the scattered radiation that

overlaps with the free electron one. The third term describes photon scattering from tightly bound electrons. In this case, electrons cannot be excited from deep states into the continuum, so the photon momentum is shared with the ion and the photons are elastically scattered.

Thus, the interplay of the scattering from all of these terms: free, tightly bound and weakly bound electrons, provides a unique method for a full characterization of the electronic state of the dense plasma. The number of valence (or delocalized) electrons can be directly inferred from the experimental spectra for the experimental conditions of this work, as well as electron temperature and density, providing important EOS model validation. We will further discuss this point using carbon as an example. By extracting carbon EOS data from experimental x-ray scattering spectra from solid density carbon plasmas, we can directly test various ionization balance models of solid density plasmas.

This paper is structured as follows. In section §II we will present the derivation of the scattering cross section including all the relevant contributions as well as corrections for strongly collisional and high density materials. Section §III will be devoted to the description of the x-ray scattering experiments on carbon solids and their interpretation. Concluding remarks will be drawn in section §IV.

## II. THEORY

Following the discussion in Ref. [1], we describe the scattering from a uniform plasma containing $N$ ions per unit volume. If $Z_A$ is the nuclear charge of the ion, the total number of electrons per unit volume in the system, including free and bound ones, is $Z_A N$. Let us now assume we probe such a system with x-rays of frequency $\omega_0$ such that $\hbar\omega_0 \gg E_I$, with $E_I$ the ionization energy of any bound electron, i.e., the incident frequency must be large compared to any natural absorption frequency of the scattering atom, which allows us to neglect resonant scattering. During the scattering process, the incident photon transfers momentum $\hbar k$ and energy $\hbar\omega = \hbar\omega_0 - \hbar\omega_1$ to the electron, where $\omega_1$ is the frequency

---

*Lawrence Livermore National Laboratory, University of California, P.O. Box 808, CA 94551
†Département de Physique Théorique et Appliquée, CEA/DAM Ile-de-France, BP12, 91680 Bruyéres-le-Châtel Cedex, France
‡Universität Rostock, Fachbereich Physik, Universitätsplatz, 3, D-18051, Rostock, Germany

of the scattered radiation, and in the non-relativistic limit ($\hbar\omega \ll \hbar\omega_0$) accounting for refractive index change:

$$k = |\mathbf{k}| = \frac{4\pi}{\lambda_0} \sin(\theta/2) \sqrt{1 - \frac{\omega_{pe}^2}{\omega_c^2}}, \qquad (1)$$

with $\lambda_0$ the probe wavelength, $\theta$ the scattering angle, $\omega_{pe} = (e^2 n_e/\epsilon_0 m_e)^{1/2}$ the electron plasma frequency and $\omega_c = 2\pi c/\lambda_0$ the critical frequency. We denote with $Z_f$ and $Z_c$ the number of kinematically free and bound electrons, respectively. Clearly, $Z_A = Z_f + Z_c$. Here $Z_c$ includes both tightly bound and weakly bound electrons. Since $Z_f$ represents electrons which are not bound to any single atom, we will also refer to it as the number of delocalized, or valence, electrons. Following the approach of Chihara [7, 8] the scattering cross section is described in terms of the dynamic structure factor of all the electrons in the plasma:

$$S(k,\omega) = |f_I(k) + q(k)|^2 S_{ii}(k,\omega) + Z_f S_{ee}^0(k,\omega)$$
$$+ Z_c \int \tilde{S}_{ce}(k,\omega - \omega') S_s(k,\omega') d\omega'. \qquad (2)$$

The first term in Eq. (2) accounts for the density correlations of electrons that dynamically follow the ion motion. This includes both the bound electrons, represented by the ion form factor $f_I(k)$, and the screening cloud of free (and valence) electrons that surround the ion, represented by $q(k)$ [9]. $S_{ii}(k,\omega)$ is the ion-ion density correlation function. The second term in Eq. (2) gives the contribution in the scattering from the free electrons that do not follow the ion motion. Here, $S_{ee}^0(k,\omega)$ is the high frequency part of the electron-electron correlation function [10] and it reduces to the usual electron feature [11, 12] in the case of an optical probe. Inelastic scattering by bound electrons is included in the last term of Eq. (2), which arises from bound-free transitions to the continuum of core electrons within an ion, $\tilde{S}_{ce}(k,\omega)$, modulated by the self-motion of the ions, represented by $S_s(k,\omega)$.

We shall also observe that for typical conditions in dense plasmas for ICF experiments, the ions are always non-degenerate, since their thermal de Broglie wavelength is much smaller than the average interparticle distance. On the other hand in the limit $T_e \rightarrow 0$, the electrons exhibit degeneracy, and obey the Fermi-Dirac distribution. In order to describe the properties of a degenerate fluid, we use the approach suggested by Dharma-Wardana and Perrot [13] of treating the correlations by considering a *classical* Coulomb fluid at some effective temperature $T_q = T_F/(1.3251 - 0.1779\sqrt{r_s})$, with $r_s = d/a_B$ ($a_B$ is the Bohr radius). The correlation properties are then calculated at the effective temperature $T_{cf} = (T_e^2 + T_q^2)^{1/2}$. This corrected temperature is chosen such that the temperature of an electron liquid obeying classical statistics exactly gives the same correlation energy of a degenerate quantum fluid at $T_e = 0$ obtained from quantum Monte Carlo calculations [14]. This approach was shown to reproduce finite-temperature static response of an electron fluid, valid

for arbitrary degeneracy [14]. The reduction to a classical electron fluid problem also allows a unified definition of the coupling constant and the scattering parameter which is valid at any degeneracy [15]. In particular, we then have $\Gamma = e^2/4\pi\epsilon_0 k_B T_{cf} d$, and similarly $\alpha = 1/k\lambda_{De} = (\epsilon_0 k_B T_{cf}/e^2 n_e k^2)^{1/2}$, i.e., with the Debye length now calculated at the temperature $T_{cf}$. In the limit $T_e \rightarrow 0$, we thus have $\alpha \sim 1/k\lambda_{TF}$.

Under these conditions, and within the framework of the density response formalism for a two component plasma, we can calculate the frequency-integrated structure factors using the semi-classical approach suggested by Arkhipov and Davletov [16], which is based on a pseudo-potential model for the interaction between charged particles to account for quantum diffraction effects (i.e., the Pauli exclusion principle) and symmetry [17–19]. The resultant expressions for the various static structures are thus:

$$S_{rs}(k) = \delta_{rs} - \frac{\sqrt{n_r n_s}}{k_B T_{cf}} \Phi_{rs}(k), \qquad (3)$$

where $r, s = e$ (electrons) or $i$ (ions), $n_e = Z_f n_i = Z_f N$ and the temperature has been assumed equal for both ions and electrons. Symmetry in the electron-ion interactions requires $S_{ei}(k) = S_{ie}(k)$. The coefficients $\Phi_{rs}(k)$ are given in Refs. [1, 16] and corresponds to Fourier transform of the screened Coulomb potentials.

Using such a model for the static properties of the plasma, we will now present simplified expressions for each term in Eq. (2) that are appropriate for low-to-mid Z, dense plasma materials.

## A. The ion feature

We will assume that the plasma has reached a state of thermodynamic equilibrium with $T_e \approx T_i$. This is justified since, for dense plasmas, the electron-ion relaxation time scales as $\sim M/2m_e\omega_{pe}$ which is typically much shorter than the characteristic lifetime of the plasma during an experiment ($\sim 1$ ns). Under these conditions, the ion motion will exhibit long-time fluctuations at the ion plasma frequency and/or sound speed. However, the frequency scale of those fluctuations is such that we are currently unable to experimentally resolve them. In this low frequency part of the spectrum, we can thus approximate $S_{ii}(k,\omega) = S_{ii}(k)\delta(\omega)$. The measured width of the feature is thus solely determined by the instrument resolution. To complete the description of the first term of Eq. (2) we need to calculate the screening charge and the ionic form factor. The screening charge is given by [7]

$$q(k) = \frac{Z_f S_{ei}(k)}{S_{ii}(k)}. \qquad (4)$$

The ionic form factor, $f_I(k)$, is related to the spatial distribution of electrons that are *truly* bound to the ions,

and it can be exactly calculated, for example, following the approach described by James [20] in the Hartree-Fock self consistent field method. This approach may be quite laborious, so, instead, hydrogenic wavefunctions with inclusion of appropriate screening constants for the bound electrons have been used to obtain the ionic form factor. As shown by Pauling and Sherman [21], this technique is fairly accurate for the low-to-mid Z elements with the advantage of simple analytical results. Typically, the contribution from K and L-shell electrons is given by

$$f_{1,0}(k) = \frac{1}{[1 + (ka_B/2Z_*)^2]^2}, \qquad (5)$$

$$f_{2,0}(k) = \frac{1 - (ka_B/2Z_*)^2}{[1 + (ka_B/2Z_*)^2]^4}, \qquad (6)$$

$$f_{2,1}(k) = \frac{[1 - 2(ka_B/2Z_*)^2][1 - (ka_B/2Z_*)^2]}{[1 + (ka_B/2Z_*)^2]^4}, \qquad (7)$$

where $Z_* = Z_A - z_{n,l}$ is the effective nuclear charge seen by the electron in the quantum state $n,l$. The screening constants $z_{n,l}$ depend on the atomic (or ionic) state of the atom and they can be calculated from the prescription of Pauling and Sherman [21]. The total ionic form factor is thus

$$f_I(k) = \sum_{n,l} f_{n,l}(k). \qquad (8)$$

For neutral isolated atoms, the ionic form factor is replaced by the atomic form factor $f_A(k)$, which is obtained for various elements, for example, from the numerical fits given by Waasmaier and Kirfel [22]. However, for plasmas and liquid metals, the approximation $f_A(k) \sim f_I(k) + q(k)$ is expected to strictly hold only in the limit [23] $k \to 0$, thus giving $f_A(k) = f_I(k) + q(k) = Z_c + Z_f = Z_A$.

## B. The electron feature

The free electron density-density correlation function that appears in the second term of Eq. (2) can be formally obtained through the fluctuation-dissipation theorem [24]:

$$S_{ee}^0(k,\omega) = -\frac{\hbar}{1 - \exp(-\hbar\omega/k_B T_e)} \frac{\epsilon_0 k^2}{\pi e^2 n_e} \text{Im}\left[\frac{1}{\epsilon(k,\omega)}\right], \qquad (9)$$

where $\epsilon(k,\omega)$ is the electron dielectric response function. In the case of an ideal classical plasma, the dielectric response is evaluated from a perturbation expansion of the Vlasov equation [25]. The resultant form for the density correlation function is then known as the Salpeter electron feature [11]. This approach, however, fails when the electrons become degenerate or nearly degenerate as

quantum effects begin to dominate. Under the assumption that interparticle interactions are weak, so that the nonlinear interaction between different density fluctuations is negligible, the dielectric function can be derived in the random phase approximation (RPA) [5, 6]. In the classical limit, it reduces to the usual Vlasov equation. We shall stress the point that the RPA is derived under the assumption $\Gamma \ll 1$, thus its validity in the description of electron correlations in weakly-to-moderate coupled systems needs to be verified.

The RPA form of the dielectric function is (see, e.g., Landau et al. [25])

$$\epsilon_{RPA}(k,\omega) = 1 - v(k)\chi_0(k,\omega), \qquad (10)$$

with $v(k) = e^2/\epsilon_0 k^2$ the Fourier transform of the bare Coulomb potential, and $\chi_0$ is the density response of the non-interacting electron system. Strong coupling effects stem from nonlinear correlations between density fluctuations and are usually described in terms of a dynamic local field correction, $G(k,\omega)$, which measures the difference between the bare Coulomb interaction and the screened response [26]

$$\chi(k,\omega) = \frac{\chi_0(k,\omega)}{1 + v(k)G(k,\omega)\chi_0(k,\omega)}, \qquad (11)$$

and, $\epsilon(k,\omega) = 1 - v(k)\chi(k,\omega)$. Clearly, the RPA is reproduced for $G(k,\omega) = 0$. The calculation of the local field correction is not an easy task, and some approximations are required. In Ref. [15] we have provided an integrated approach to obtain local field corrections within the density response formalism. In the small $\alpha$ regime which is relevant to the experiments described in this paper, we showed that the corrections to the RPA introduced by the local field are indeed negligible.

## C. The bound-free feature

In Ref. [1], we have presented simplified expressions for the last term in Eq. (2) for low-Z materials. In those cases, the bound-free contribution is small under most experimental conditions and it can be neglected. However, in the case of carbon, L-shell inelastic scattering needs to be included. Differently from the approach followed in Ref. [1], we propose a more comprehensive treatment of the core electron term based on the impulse approximation (IA) [27, 28]. The IA assumes that the electron-photon interaction occurs on a very short time-scale, so the target electron always sees the same nuclear potential just before and after the collision. Since only changes in the kinetic energy needs to be considered, the electron can be treated as free and its final energy depends on the projection of the electron's initial momentum on the scattering vector $\mathbf{k}$. Thus, the Doppler broadening of the scattered radiation is proportional to the initial momentum distribution of the electron [29]. In the hydrogenic

approximation for the initial wavefunction and momentum distribution of the electron, the IA profiles for K and L-shells assume the form [30]

$$J_{1,0}^0(\xi) = \frac{8}{3\pi Z_*(1 + \xi^2/Z_*^2)^3}, \qquad (12)$$

$$J_{2,0}^0(\xi) = \frac{64}{\pi Z_*}\left[\frac{1}{3(1 + 4\xi^2/Z_*^2)^3}\right.$$
$$\left. -\frac{1}{(1 + 4\xi^2/Z_*^2)^4} + \frac{4}{5(1 + 4\xi^2/Z_*^2)^5}\right], \qquad (13)$$

$$J_{2,1}^0(\xi) = \frac{64}{15\pi Z_*}\frac{1 + 20\xi^2/Z_*^2}{(1 + 4\xi^2/Z_*^2)^5}, \qquad (14)$$

where,

$$\xi = \frac{m_e a_B}{\hbar k}\left(\omega - \frac{\hbar k^2}{2m_e}\right). \qquad (15)$$

As discussed by Eisenberger and Platzman [27], the IA is correct to the order of $|E_B/E_c|^2$, where $E_B$ is the binding energy and $E_c$ is the Compton recoil. For our typical experimental conditions the Compton recoil, $E_c = \hbar^2 k^2/2m_e \sim 70$ eV and the binding energy of L-shell carbon electrons is $|E_B| \sim 11\text{-}64$ eV (depending on the ionization state), thus errors introduced by the IA can be significant. Even if K-shell contribution is typically less important than the L-shell one, corrections to the IA need to be accounted for K-shell electrons as well. The main modification in the IA appears as a shift of the peak of feature from the free electron value, an effect known as the Compton defect (see e.g., [31, 32]). Since the IA assumes plane waves as the final state for the electron, improvement in the model can be obtained by using the first Born approximation and hydrogenic wavefunctions for both initial and final states [27, 33, 34], or by a perturbation expansion of the final states [35, 36]. In our work we will follow the perturbative approach of Holm and Ribberfors [36] which gives for the first order asymmetric correction to the IA:

$$J_{1,0}^1(\xi) = J_{1,0}^0(\xi)\frac{Z_*}{ka_B}\left[\frac{3}{2}\xi - 2\text{atan}(\xi)\right], \qquad (16)$$

$$J_{2,0}^1(\xi) = J_{2,0}^0(\xi)\frac{Z_*}{ka_B}\left[\frac{5}{4}\frac{1 + 48\xi^4}{1 - 10\xi^2 + 40\xi^4}\xi - 2\text{atan}(2\xi)\right], \qquad (17)$$

$$J_{2,1}^1(\xi) = J_{2,1}^0(\xi)\frac{Z_*}{ka_B}\left[\frac{2}{3}\frac{10 + 60\xi^2}{1 + 20\xi^2}\xi - 2\text{atan}(2\xi)\right], \qquad (18)$$

with the corrected IA profiles given by $J_{n,l}(\xi) = J_{n,l}^0(\xi) + J_{n,l}^1(\xi)$. Even if such modified IA expressions already provide accurate profiles for the experimental conditions of interest, further improvements to the IA can be obtained

if more realistic wavefunctions (such as Hartree-Fock) are used instead of hydrogenic ones (see e.g., [31]). For L-shell electrons and atoms in their neutral state, the error introduced by the hydrogenic wavefunctions is $\lesssim 10\%$ when compared to Hartree-Fock wavefunctions [37] for our typical experimental conditions. Since $ka_B/Z_A \lesssim 1$, additional corrections can be necessary for the K-shell electrons if we want to account for scattering events that involve a transition from a 1s state to an unoccupied orbital in a Raman-type process [38–40]. Considering the fact, as we will see shortly, that K-shell scattering is a minor effect in the overall spectrum, in this work we will regard Raman-type transitions as an higher order correction and we will not include them in the core electron scattering form factor.

Bound-free transitions are not energetically allowed if energy transfered from the photon to the electron is less that the energy of the bound state, i.e., $\hbar\omega < |E_B|$. Thus the dynamic structure has a cut-off at the ionization energy for K and L-shell electrons. Partial bound-free IA static structure factors, defined as

$$\sigma_{n,l}(k) = \int_{eE_B/\hbar}^{eE_0/\hbar} J_{n,l}(\xi)d\omega \sim \int_{eE_B/\hbar}^{\infty} J_{n,l}(\xi)d\omega, \qquad (19)$$

are plotted in Fig. 1, as a function of $E_B/E_c = E_B\hbar^2 k^2/(2m_e)$ for neutral carbon. We have also set $E_B$ equal to the Compton energy that corresponds to a scattering angle $\theta = 130°$ with a probe energy $E_0 = 4.75$ keV. Since the binding energy $E_B$ gives only the position of the cut-off in the scattering cross section, the profiles of Fig. 1 are self-similar with respect to $E_B$ and they can be rescaled for different values of the binding energy. Since $E_B$ for L-shell electrons in significantly smaller than for K-shell electrons, we see that a large fraction of the total bound-free structure is determined by the electrons in the outermost shells. These results are also weakly dependent on $Z_*$ and similar plots apply for higher ionization states.

The total bound-free dynamic structure, as it appears in Eq. 2, is thus written as

$$\tilde{S}_{ce}(k, \omega) = \frac{r_k}{Z_c B^3}\sum_{n,l} J_{n,l}(\xi), \qquad (20)$$

with the sum running over all the bound electrons. The normalization constant $r_k$ accounts for the possibility of coherent scattering [41] and it is given by [20]

$$r_k = 1 - \frac{1}{Z_c}\sum_n f_n^2(k) \sim 1 - \frac{|f_I(k)|^2}{Z_c^2}, \qquad (21)$$

where $f_n(k)$ are the partial form factors for each bound electron [21] and $\sum_n f_n(k) = f_I(k)$. The coefficient $B$ in Eq. (20) is only important for very large momentum transfer and it is given by the Breit-Dirac formula [20]

$$B = 1 + \frac{1}{\omega_0}\frac{\hbar k^2}{2m_e}. \qquad (22)$$

In the high frequency limit, the ion-ion self structure is $S_s(k,\omega) \sim \delta(\omega)$, as ion dynamics remain unresolved under our experimental conditions [1]. Profiles of the bound-free dynamic structure, $\tilde{S}_{ce}(k,\omega)$, for a carbon plasma are given in Fig. 2 for different ionization states and typical experimental conditions. The carbon is assumed to be in an amorphous state (foam) with density 0.72 g/cc. We clearly see in Fig. 2 the cut-off at the ionization energy for L-shell electrons, and similarly, for K-shell electrons, the cut-off marks the K-shell binding energy.

In the case of very dense plasmas, the potential distribution of a given ion is influenced not only by its own bound electrons but also by the neighboring ions. The net effect is a lowering of the ionization potential (*continuum lowering*). Such lowering depends on the total number of ions that participate in the modification of the potential around a test ion, which, in turn, is a function of the screening distance of the Coulomb forces. Stewart and Pyatt [42] have calculated the continuum lowering using a finite-temperature Thomas-Fermi model which reproduces both the classical Debye screening for low density plasmas and the ion-sphere correlation length for high density coupled systems. In their model, the lowering of the ionization potential is given by:

$$\Delta E_B = \frac{Z_f e^2}{(4\pi\epsilon_0)\lambda_s},$$ (23)

with,

$$\lambda_s = \frac{2}{3} \frac{Z_f^{1/3} d \left( \frac{Z_f^{1/3} d}{\lambda_D} \right)^2}{\left[ \left( \frac{Z_f^{1/3} d}{\lambda_D} \right)^3 + 1 \right]^{2/3} - 1},$$ (24)

and $\lambda_D = \sqrt{\epsilon_0 k_B T_{cf}/n_e(Z_f + 1)e^2}$ is the Debye length which includes both the electron and the ion response. For typical experimental conditions, $\Delta E_B$ accounts for $\sim$30-50% of the ionization energy, thus continuum lowering strongly shifts the L-shell edges of the bound-free dynamic structure. Experimental verification of this model for continuum lowering was presented by Bradley *et al.* [43] with time-resolved continuum-edge shift measurements in laser-shocked plasmas. The *effective* ionization energy is thus determined as $E_B = E_B^0 - \Delta E_B$, where $E_B^0$ is the ionization energy of an isolated atom. $E_B^0$ values for L-shell electrons for atoms in different ionization stages are obtained from tabulated data [44], and for K-shell electrons from the fitting formula given by Band *et al.* [45].

It is interesting to compare the total scattered power by bound and free electrons in the elastic and inelastic terms. By integrating over frequencies Eq. (2) we obtain the total static structure

$$S(k) = S_I(k) + S_E(k) + S_C(k),$$ (25)

where,

$$S_I(k) = |f_I(k) + q(k)|^2 S_{ii}(k),$$ (26)

$$S_E(k) = Z_f S_{ee}^0(k),$$ (27)

with,

$$S_{ee}^0(k) = S_{ee}(k) - \frac{|q(k)|^2}{Z_f} S_{ii}(k);$$ (28)

and,

$$S_C(k) = \frac{r_k}{B^3} \sum_{n,l} \sigma_{n,l}(k).$$ (29)

The total elastic component of the scattered x-ray radiation is $S_I(k)$ and it includes contribution from both free and bound electrons. Inelastic scattering by free electrons and bound electrons is given by the terms $S_E(k)$ and $S_C(k)$, respectively. In Fig. 3 we have plotted as a function of the charge state the various static structure for a carbon plasma, 0.72 g/cc, $T_e = 20$ eV, probed with x-rays of energy $E_0 = 4.75$ keV at 130° scattering angle. We see that for $Z_f \lesssim 3$, the amount of the scattered radiation by bound-free transitions is quite large and it must be considered for a correct evaluation of the experimental profiles, if accurate measurements of the electron density, electron temperature and charge state are to be performed.

## III. EXPERIMENTAL RESULTS

We apply the calculation technique discussed in the previous section to a dense carbon plasma. We used the 30-kJ Omega laser facility [46] to produce a homogeneous and isochorically heated carbon plasma at solid density, and then probed the plasma interior with the Ti He-$\alpha$ x-ray line at 4.75 keV from a secondary laser produced plasma. The details of the experimental technique have been extensively discussed in Refs. [2, 3]. Prior to laser heating, the carbon is in an amorphous (foam) state with density 0.72 g/cc. Since during the heating and probing times the plasma is not globally expanding (see Ref. [3]), the initial carbon density sets the ion density to $n_i = 3.6 \times 10^{22}$ cm$^{-3}$. The electron density is then determined by the ionization state of the system. Uniform ( in $T_e$ and $n_e$) and isochoric heating has been also confirmed by both numerical simulations and spectrally integrated x-ray framing images of the samples, as shown by Glenzer *et al.* [2]. By changing the number of heating beams, we can vary the degree of carbon heating and consequently its ionization state.

In Fig. 4 we have plotted experimental profiles obtained for two different cases: a strongly heated foam and a cold one. The scattered radiation has been collected at $\sim$ 130° $\pm$ 5° scattering angle with a high efficiency graphite Bragg crystal operated in mosaic focusing

mode. This geometry corresponds to a scattering parameter $\alpha < 1$, thus the scattering is noncollective and the spectra of the free electrons directly represent the electron velocity distribution function [1]. As an additional remark, we notice that for our experimental conditions, the electron-electron coupling constant $\Gamma \lesssim 1$, thus local field corrections to the RPA are not important, as previously observed. From Fig. 4 we notice an increased red wing for the higher temperature foam, indicating a higher $T_e$ plasma with more free electrons and higher ionization state. By combining the theory outlined in the previous section for the core electrons and by assuming that the free electron response can be described within the RPA, we can fit the experimental data to obtain $T_e$ and $Z_f$. The electron density is then simply given as $n_e = Z_f n_i$, as heating is isochoric and the plasma does not expand at the probing time. The high temperature foam gives $Z_f = 4.25$ and $T_e = 52$ eV, while for the cold foam $Z_f = 0.26$ and $T_e = 5$ eV. As discussed by Glenzer et al. [2], the errors in the temperature and density measurements for the high temperature foam are $\lesssim 20\%$. This is clearly shown in Fig. 5, where we plot the quality of the data fitting as measured by the parameter

$$\chi^2 = \sum_{i=1}^{m} \left[ A_G(k) S(k, \omega_i) - y_i \right]^2 , \qquad (30)$$

where the sum extends to all the $m$ data points, with $y_i$ the measured intensity at the frequency $\omega_i$, and $A_G(k)$ is a geometrical factor that accounts for the overall instrument response. The plot in Fig. 5a is obtained by arbitrarily varying $T_e$ and $Z_f$ in the total form factor (2). We see that by covering a large parameter space in temperature and ionization states, $\chi^2$ shows a unique minimum thus confirming the small errors in the measurements.

For the cold foam, the electron plasma is partially degenerate $(T_e \sim T_F)$ and the width of the Compton feature is only weakly sensitive on the electron temperature. Moreover, the Compton profile mainly results from bound-free transitions which directly reflects the bound electron momentum. Under these conditions, the fitted temperature is understood only as an upper limit of the actual electron temperature of the degenerate electron fluid. Fig. 5b shows the $\chi^2$ density plot for a range of electron temperatures and ionization states.

Differently from the high temperature case, we now see the appearance of two local minima. Physical reasoning, however, limits the possible solutions. In the cold experiment, heating of the carbon foam is very minimal and it can only be induced by the probe itself. Comparison with numerical simulations suggests that such an effect cannot account for more than a few eV's, thus excluding the high temperature minimum in the $\chi^2$ plot. Fig. 5b also shows that a typical error in the ionization state value is less than $\pm 0.5$. Differently from the high temperature foam, where the red wing of the spectrum is mainly due to free electron scattering [3], in the cold foam experiment, scattering from weakly bound (L-shell) electrons

represents the dominant contribution to the red wing. This is elucidated in the plot of Fig. 6. We should also note that, since the width of the free electron feature is proportional to $T_{cf}^{1/2}$ [1], while the width of the bound-free feature depends on the bound electron momentum, we cannot simply fit the low temperature experimental data by assuming a larger ionization state $(Z_f)$ with no bound-free contribution. This, as well, explains the importance of L-shell electron scattering in determining the lineshape.

Fig. 7 compares the ionization balance vs $T_e$ with experimental data and various EOS models for carbon. The third data point, at intermediate $T_e$, was obtained by heating the plasma with a lower number of driver beams. The models compared in the figure are the activity expansion method (ACTEX) [47, 48], the partially ionized plasma (PIP) model [49, 50] and SCAALP, a density functional plasma model [51]. In the ACTEX theory, all possible interactions between plasma constituents are calculated including the screening of the bound states. For large densities, the classical Debye-Hückel (Yukawa) potential is replaced by a screened potential which has a cut-off for distances that approach the thermal de Broglie wavelength, in order to mimic quantum mechanical effects (i.e., exchange and symmetry). This approach allows the calculation of de-localized electrons, i.e., the number of electrons that are no longer bound to a single ion. These electrons are free or weakly bound, like the conduction electrons in a metal. For our conditions, these electrons give rise to the Compton downshifted electron feature of the x-ray scattering spectrum. The PIP model is based on the self-consistent solution of Saha-like equations for each ionization stage together with the calculation of appropriate chemical potentials for electrons and ions. This also allows the inclusion of high density effects by using corrected chemical potentials for the continuum lowering. SCAALP is based on the density functional theory for plasmas, where electronic structure and ionic distribution are determined self-consistently. The plasma is considered as an effective classical system of virtual neutral particles (neutral pseudo-atom, NPA) interacting via an interatomic effective potential $\phi(r)$. Electrons of the NPA satisfy a Schrodinger equation with an effective central symmetric potential $V_{eff}(r)$. Both $V_{eff}$ and $\phi$ are determined by the electronic structure and the ionic distribution of the plasma. Polarization and correlation effect of the continuum electrons are taken into account, as well as a part of the exchange interaction within both $V_{eff}(r)$ and $\phi(r)$.

Results from these models, assuming different values for the carbon density, are plotted in Fig. 7. The comparison with the experimental data shows good agreement with SCAALP at all densities, even if some differences still remain especially for the high temperature case. The PIP model also gives reasonably good agreement with the data at all densities, but it seems to over-predict the ionization state in the mid-temperature regime. In this regime, the influence of quantum mechanical corrections

to the ideal Saha equations used in various approaches is important. ACTEX shows a similar trend to SCAALP for the low density simulation, but, in the higher density case, predicts a low temperature foam which has ~2 electrons in the conduction band. This transition to a metallic state for carbon at high density are not reproduced by the other models at this density. Our experimental data at low $T_e$ show an insulating behavior for carbon at high density.

From this discussion, we see that currently available EOS models for carbon exhibit different behavior in the temperature range 0-50 eV, which span the range from fully degenerate to classical plasmas. X-ray scattering thus provides an accurate experimental tool for validation and improvement of EOS codes, as shown in Fig. 7.

## IV. CONCLUSIONS

In this paper we have provided expressions used to calculate the x-ray scattering form factor for moderate to low-Z materials, including the contribution of both weakly and tightly bound electrons, and free electrons as well. The approach used for weakly bound electrons is based on the IA corrected for the asymmetry induced by the electron binding, accounting for pressure ionization in high density systems. The free electron feature is evaluated from ideal classical plasmas to strongly coupled and degenerate systems. We then show that the RPA is accurate for the plasma regimes covered in experiments performed at the Omega laser facility. We have fitted our model to the experimental data in order to extract accurate values for electron temperature and ionization state for a solid density carbon plasma. This has allowed the comparison various ionization balance models with our data, thus enabling a direct validation of EOS theories for a carbon plasma in a regime which cover the transition between a degenerate to classical fluid. Our result are of interest for ICF research as well as planetary science since they indicate that matter under extreme conditions, as the one found in fuel pellet during compression or in the interior of planets, can now be investigated with good accuracy.

[1] G. Gregori, S. H. Glenzer, W. Rozmus, R. W. Lee, and O. L. Landen, Phys. Rev. E **67**, 026412 (2003).
[2] S. H. Glenzer, G. Gregori, R. W. Lee, F. J. Rogers, S. W. Pollaine, and O. L. Landen, Phys. Rev. Lett. **90**, 175002 (2003).
[3] S. H. Glenzer, G. Gregori, F. J. Rogers, D. H. Froula, S. W. Pollaine, R. S. Wallace, and O. L. Landen, Phys. Plasmas **10**, 2433 (2003).
[4] J. D. Lindl, *Inertial Confinement Fusion* (Springer-Verlag, New York, 1998).
[5] D. Pines and D. Bohm, Phys. Rev. **85**, 338 (1952).
[6] D. Pines and P. Nozieres, *The Theory of Quantum Fluids* (Addison-Wesley, Redwood, CA, 1990).
[7] J. Chihara, J. Phys. F: Met. Phys. **17**, 295 (1987).
[8] J. Chihara, J. Phys.: Condens. Matter **12**, 231 (2000).
[9] D. Riley, N. C. Woolsey, D. McSherry, I. Weaver, A. Djaoui, and E. Nardi, Phys. Rev. Lett. **84**, 1704 (2000).
[10] S. Ichimaru, *Basic Principles of Plasma Physics* (Addison, Reading, MA, 1973).
[11] E. E. Salpeter, Phys. Rev. **120**, 1528 (1960).
[12] D. E. Evans and J. Katzenstein, Rep. Prog. Phys. **32**, 207 (1969).
[13] F. Perrot and M. W. C. Dharma-Wardana, Phys. Rev. B **62**, 16536 (2000).
[14] M. W. C. Dharma-Wardana and F. Perrot, Phys. Rev. Lett. **84**, 959 (2000).
[15] G. Gregori, S. H. Glenzer, and O. L. Landen, J. Phys. A: Math Gen. **36**, 5971 (2003).
[16] Y. V. Arkhipov and A. E. Davletov, Phys. Lett. A **247**, 339 (1998).
[17] C. Deutsch, Phys. Lett. **60A**, 317 (1977).
[18] C. Deutsch, M. M. Gombert, and H. Minoo, Phys. Lett. **66A**, 381 (1978).
[19] C. Deutsch, M. M. Gombert, and H. Minoo, Phys. Lett. **72A**, 481 (1981).
[20] R. W. James, *The Optical principles of the Diffraction of X-rays* (Ox Bow Press, Woodbridge, CT, 1962).
[21] L. Pauling and J. Sherman, Zeit. f. Krist. **1**, 81 (1932).
[22] D. Waasmaier and A. Kirfel, Acta Cryst. A **51**, 416 (1995).
[23] J. A. Anta and A. A. Louis, Phys. Rev. B **61**, 11400 (2000).
[24] R. Kubo, J. Phys. Soc. Japan **12**, 570 (1957).
[25] L. D. Landau, E. M. Lifshitz, and L. P. Pitaevskii, *Physical Kinetics* (Pergamon, Oxford, 1995).
[26] S. Ichimaru, *Statistical Plasma Physics* (Addison-Wesley, Reading, MA, 1991).
[27] P. Eisenberger and P. M. Platzman, Phys. Rev. A **2**, 415 (1970).
[28] R. Currat, P. D. DeCicco, and R. Kaplow, Phys. Rev. B **3**, 243 (1971).
[29] J. W. M. DuMond, Phys. Rev. **29**, 643 (1929).
[30] B. J. Bloch and L. B. Mendelsohn, Phys. Rev. A **12**, 1197 (1975).
[31] P. M. Bergstrom and R. H. Pratt, Radiat. Phys. Chem. **50**, 3 (1997).
[32] A. Issolah, B. Levy, A. Beswick, and G. Loupias, Phys.

Rev. A **38**, 4509 (1988).

[33] F. Bell, J. Chem. Phys. **85**, 303 (1986).

[34] B. J. Bloch and L. B. Mendelsohn, Phys. Rev. A **9**, 129 (1974).

[35] F. Gasser and C. Tavard, Phys. Rev. A **27**, 117 (1983).

[36] P. Holm and R. Ribberfors, Phys. Rev. A **40**, 6251 (1989).

[37] Y. F. Chen, C. M. Kwei, and C. J. Tung, Phys. Rev. A **47**, 4502 (1993).

[38] Y. Mizuno and Y. Ohmura, J. Phys. Soc. Japan. **22**, 445 (1967).

[39] T. Suzuki, J. Phys. Soc. Japan **22**, 445 (1967).

[40] T. Suzuki, A. Tanokura, and N. Arimitsu, J. Phys.: Condens. Matter **1**, 5187 (1989).

[41] T. Paakkari and P. Suortti, Phys. Rev. B **9**, 1756 (1974).

[42] J. C. Stewart and K. D. Pyatt, ApJ **1203**, 144 (1966).

[43] D. K. Bradley, J. Kilkenny, S. J. Rose, and J. D. Hares, Phys. Rev. Lett. **59**, 2995 (1987).

[44] R. L. Kelli, J. Phys. Chem. Ref. Data **16**, 1 (1987).

[45] I. M. Band, M. B. Trzhaskovskaya, D. A. Verner, and D. G. Yakovlev, Astron. Astrophys. **267**, 237 (1990).

[46] J. M. Soures *et al.*, Fusion Technol. **30**, 492 (1996).

[47] F. J. Rogers and D. A. Young, Phys. Rev. E **56**, 5876 (1997).

[48] F. J. Rogers, Phys. Plasmas **7**, 51 (2000).

[49] S. Kuhlbrodt and R. Redmer, Phys. Rev. E **62**, 7191 (2000).

[50] R. Redmer, Phys. Rev. E **59**, 1073 (1999).

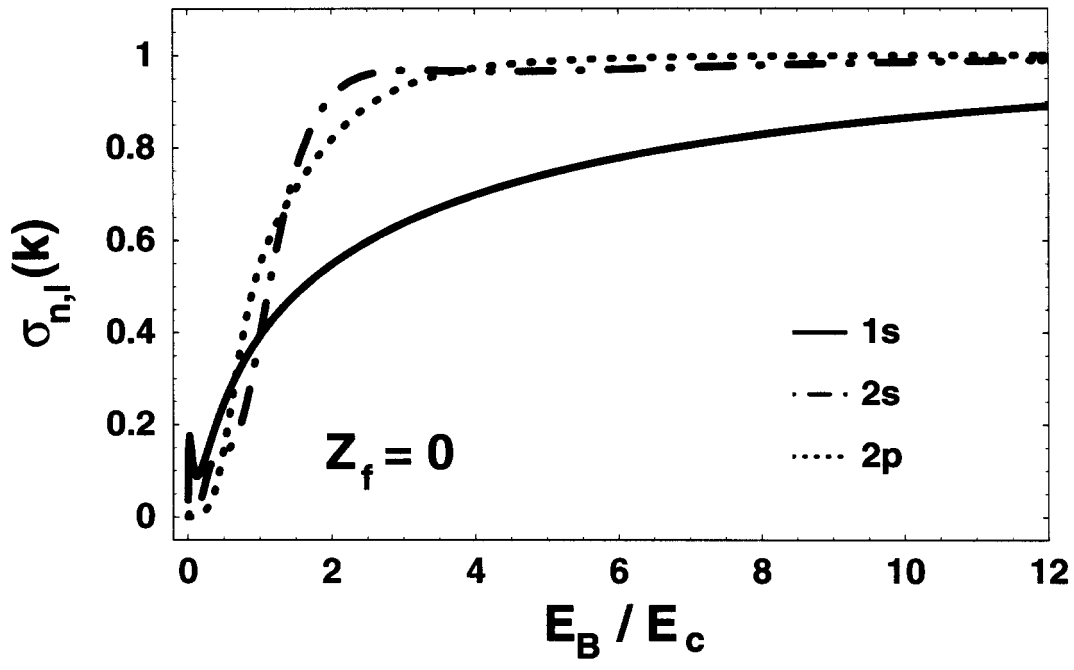[51] P. Renaudin, C. Blancard, G. Faussurier, and P. Noiret, Phys. Rev. Lett. **88**, 215001 (2002).

FIG. 1: Partial bound-free IA static structure factors $\sigma_{n,l}(k)$ for neutral carbon. $E_c$ is the Compton recoil.
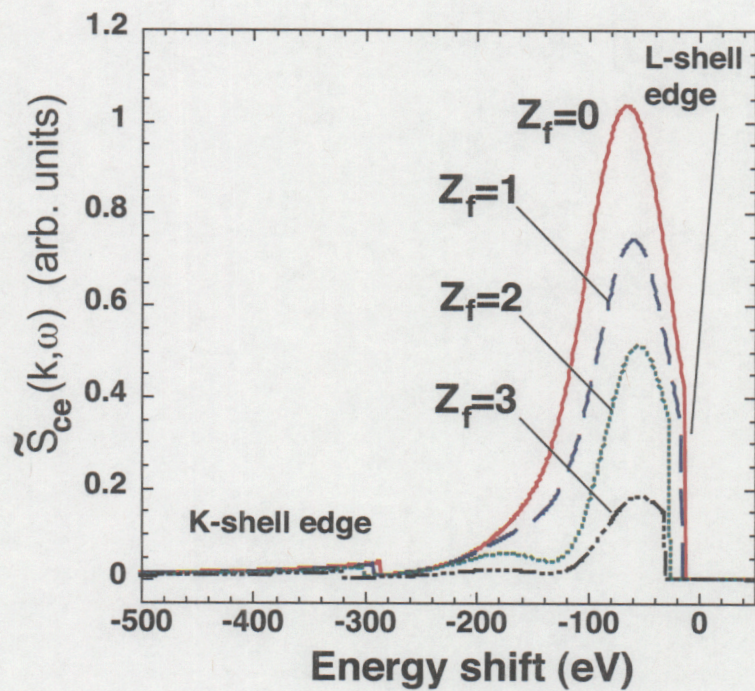
FIG. 2: (color) Calculated bound-free dynamic structures, $\tilde{S}_{ce}(k,\omega)$, for a carbon plasma with density 0.72 g/cc at 130° scattering angle. The probe energy is $E_0 = 4.75$ keV. The ionization energy is corrected for continuum lowering.
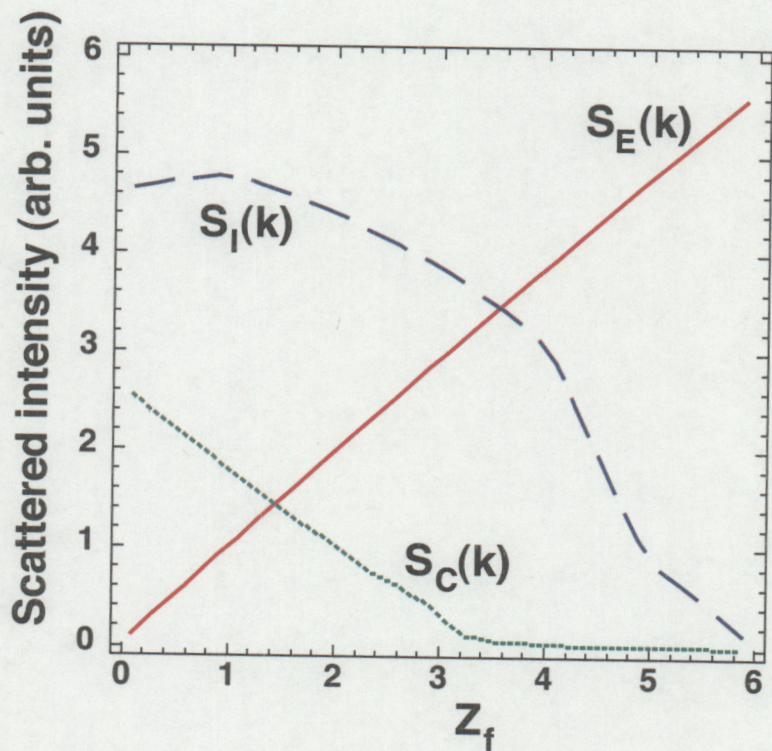
FIG. 3: (color) Static structures obtained for a carbon plasma with density 0.72 g/cc and $T_e = 20$ eV. The probe radiation is $E_0 = 4.75$ keV and the scattering angle is 130°.
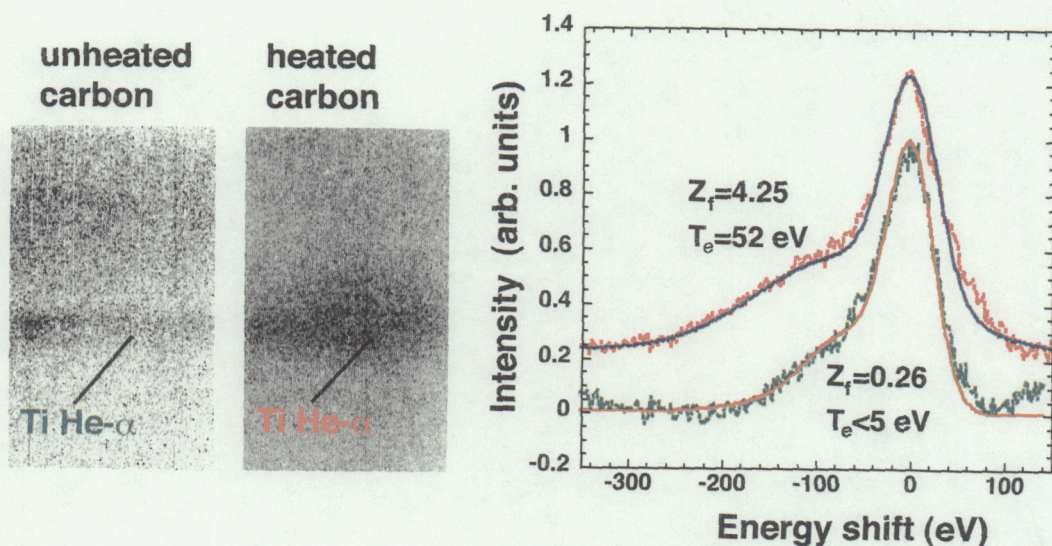
FIG. 4: (color) Experimental x-ray scattering data from a heated carbon foam (0.72 g/cc) and a cold (unheated) carbon foam. The raw data, as measured by the detector are shown on the left side. Lineouts and best fits are reported on the right panel. The probe radiation is the Ti He-$\alpha$ line at 4.75 keV, and the scattered x-rays are collected at $\sim 130° \pm 5°$ scattering angle. Best fit parameters and corresponding spectra are also plotted in the figure. For the high temperature foam, $\alpha = 0.17$, $T_F = 10.4$ eV, and $\Gamma = 0.2$; while for the cold foam $\alpha = 0.13$, $T_F = 1.6$ eV, and $\Gamma = 0.9$.
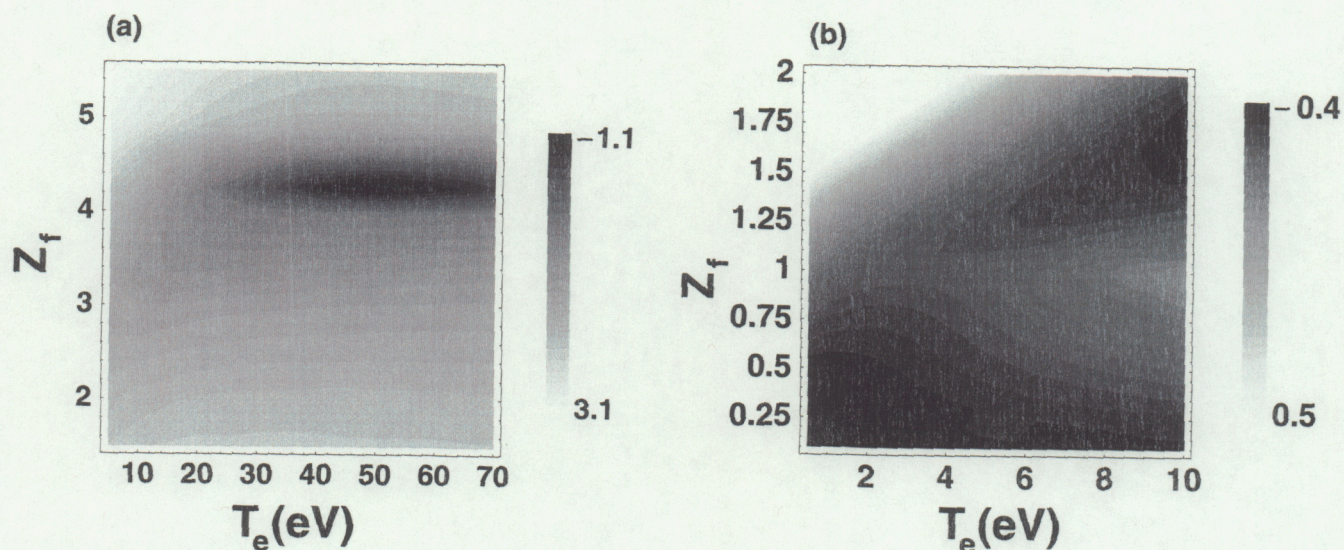


FIG. 5: $\chi^2$ mapping (log scale). (a) high temperature carbon foam experiment. Best fit corresponds to $T_e = 52$ eV and $Z_f = 4.25$. (b) old carbon foam experiment. Best fit corresponds to $T_e < 5$ eV and $Z_f = 0.26$.
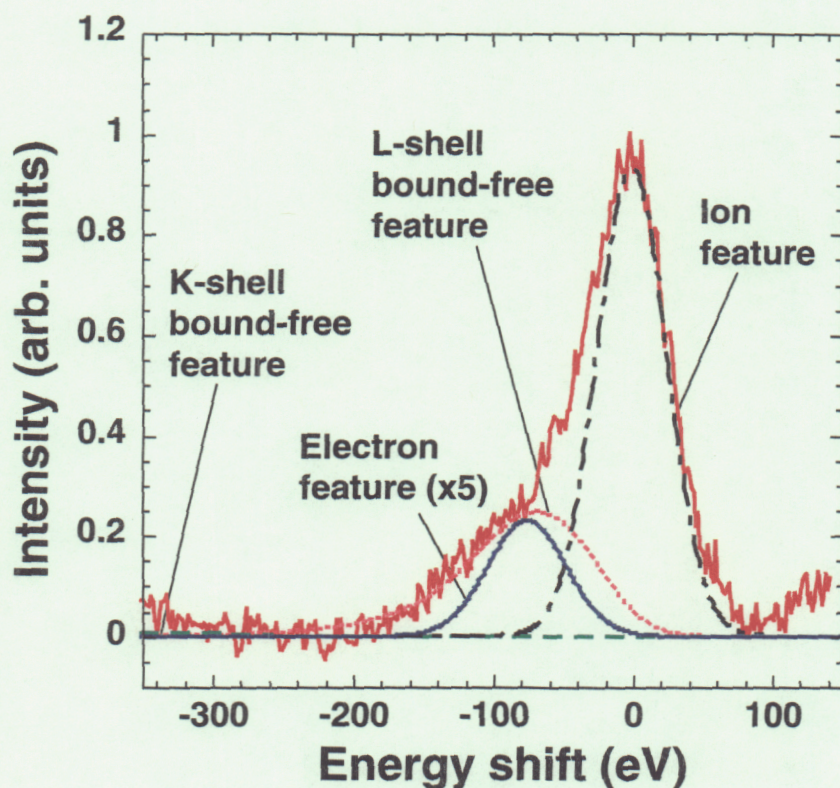
FIG. 6: Spectrum of the unheated foam with separated contributions from each different scattering mechanism. Convolution with instrument response is added each terms. The probe radiation is the Ti He-$\alpha$ line at 4.75 keV, and the scattered x-rays are collected at $\sim 130° \pm 5°$ scattering angle with best fit parameters $T_e < 5$ eV and $Z_f = 0.26$. The ionization energy for isolated neutral carbon is $E_B^0 = 11$ eV for L-shell electrons and $E_B^0 = 286$ eV for K-shell electrons.
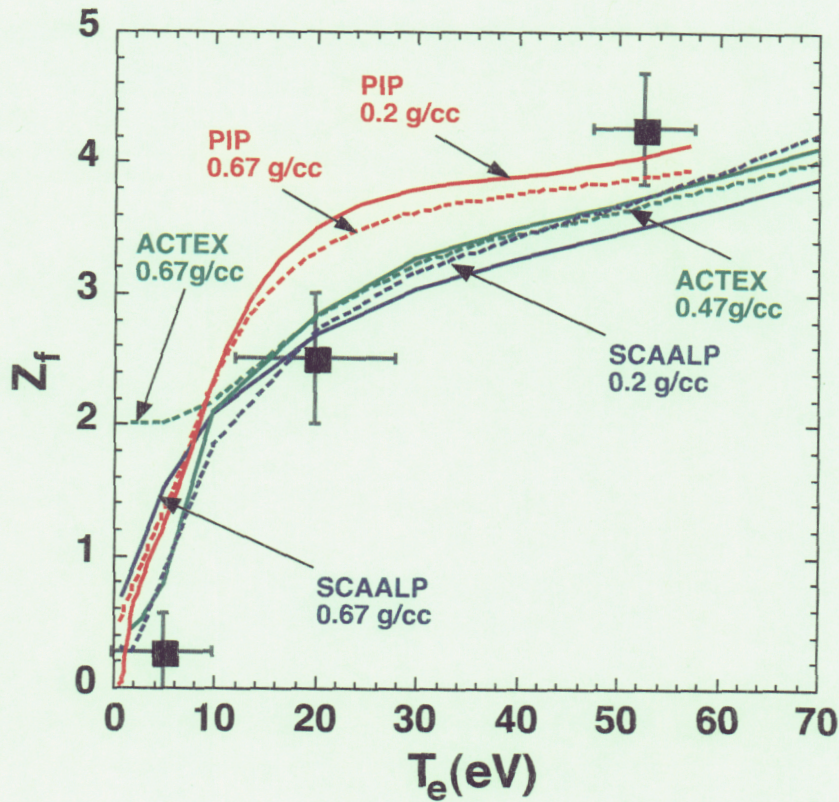
FIG. 7: (color) Temperature-ionization diagram along with the results of the x-ray scattering measurements and various EOS models. ACTEX with carbon density $\rho = 0.67$ g/cc (solid green line), ACTEX with carbon density $\rho = 0.47$ g/cc (dotted green line), PIP with carbon density $\rho = 0.67$ g/cc (solid red line), PIP with carbon density $\rho = 0.2$ g/cc (dotted red line), SCAALP with carbon density $\rho = 0.67$ g/cc (solid blue line), and SCAALP with carbon density $\rho = 0.2$ g/cc (dotted blue line)